ROYAL SOCIETY OF CHEMISTRY

PAPER

Check for updates

The preparation route and final form of V-MXenes override the effect of the O/F ratio on their magnetic properties†

Pavla Eliášová, [ID] *[a] Břetislav Šmíd, [ID] [b] Jana Vejpravová, [ID] [b] Shuo Li,[a] Federico Brivio,[a] Michal Mazur, [ID] [a] Daniel N. Rainer,[a] M. Infas H. Mohideen,[a] Russell E. Morris [ID] [c] and Petr Nachtigall [ID] ‡[a]

Transition metal carbides and nitrides (MXenes) show a high potential for electrochemical energy storage in batteries and supercapacitors and for electrocatalysis. Their excellent electronic and magnetic characteristics have been highlighted in several theoretical studies. However, experimental research on MXenes is yet to confirm their predicted properties as candidates for controllable magnetic 2D materials. Here, we report our theoretical and experimental study of V_2CT_x MXenes (T = O, OH, F), providing key insights into their magnetism. Based on our density functional theory (DFT) analysis, we predicted ferromagnetic (FM) and antiferromagnetic (AFM) states of V_2CT_x, which are determined by the O/F ratio of surface functional groups. Accordingly, we prepared V_2CT_x MXenes in the form of multilayered powders and thin films with different O/F ratios. No experimental evidence of FM or AFM properties was found in any material. Nevertheless, powders and films with almost identical chemical compositions (in terms of O/F ratio) displayed different magnetic properties, whereas films with disparate chemical compositions revealed a similar magnetic character. Therefore, the preparation route and form of the final V_2CT_x material override the effect of the O/F ratio, which is often overestimated in theoretical studies. Moreover, these findings underscore the importance of preparing MXene materials to experimentally confirm their theoretically predicted properties.

Introduction

Isolated graphene layers have opened up many opportunities for new discoveries.[1] As a result, considerable research efforts have focused on two-dimensional (2D) materials. Thanks to their distinctive properties, 2D materials such as transition metal oxides,[2] hexagonal boron nitrides,[3] transition metal dichalcogenides[4] and clays[5] can be used in a wide range of technological applications, including gas sensors, materials for energy storage, field-effect transistors (FETs) and photodetectors, and in medicine as drug delivery agents, respectively. In particular, the ability to prepare layered $Ti_3C_2T_x$[6] has fostered numerous new 2D metal carbides and nitrides (MXenes).[7]

MXenes display high electrical conductivity, redox active surface area and mechanical strength, in addition to rich surface chemistry. These properties endow MXenes with a high potential for many applications. As a case in point, these materials have been extensively studied for electrochemical energy storage applications, such as lithium-ion batteries,[8] and electrochemical capacitors,[9] and for photovoltaic applications.[10] Furthermore, MXenes have been tested in electrocatalytic oxygen and hydrogen evolution and CO_2 reduction,[11] water desalination[12] and, more recently, electromagnetic interference (EMI) shielding.[13]

MXenes have an $M_{n+1}X_n$ general formula where M is a transition metal, and X stands for carbon or nitrogen. Only MXenes with M = Ti, V, Nb, Mo, Cr, Hf, Sc, Ta, W, or Y have been reported thus far, most of which prepared by wet-etching the aluminium layer of a parent MAX phase with a general formula of $M_{n+1}AX_n$, where A represents elements of groups 13 and 14 of the periodic table, primarily aluminium. After aluminium removal, the surface of MXenes becomes covered by mixed terminations. MXenes are then designated by $M_{n+1}XT_x$, where T can be O, OH, NH, F, Cl, Br, S, Se, or Te, depending on the etching[14,15] and post-etching procedures.[16–19] Typically,

[a] Faculty of Sciences, Charles University, Hlavova 8, Prague 2 128 43, Czech Republic. E-mail: pavla.eliasova@natur.cuni.cz

[b] Faculty of Mathematics and Physics, Charles University, Ke Karlovu 5, Prague 2 121 16, Czech Republic

[c] EaStCHEM School of Chemistry, University of St. Andrews, St. Andrews KY16 9ST, UK

† Electronic supplementary information (ESI) available. See DOI: https://doi.org/10.1039/d4tc00132j

‡ Deceased.

these etching procedures involve using (concentrated or *in situ*-formed) hydrofluoric acid and/or hydrochloric acid, which lead to O, OH, F and Cl terminal groups. In just over a decade, more than 30 stoichiometric MXenes have been synthesized, and more than a hundred MXenes (disregarding variable surface terminations) have been theoretically predicted.[20,21] As one of the fastest growing class of 2D materials,[7] MXenes have been the object of research of many theoretical studies, predicting excellent electronic and magnetic characteristics. For these properties, they stand out as ideal candidates for controllable magnetic 2D materials.[21–26]

Most pristine and functionalized MXene materials are non-magnetic due to strong covalent bonding between the transition metal and the X element and to surface functional groups, as shown by density functional theory (DFT) calculations.[27] Conversely, MXenes based on Cr, V and/or Mn should be magnetically active, according to theoretical predictions.[21,23–25,28,29] But whether symmetrical or asymmetrical with respect to the upper and lower surfaces, surface functionalization of these materials (*e.g.*, F, O or OH) likely changes their magnetic properties. For example, Mn_2CF_2 is an intrinsic half-metal with a high Curie temperature (520 K), which can be used for spin injection in spintronics,[24] and functionalized M_2N (M = Mn, Cr and Ti) MXenes are half-metallic as well.[30] So, half-metal materials, which are metallic in one spin channel and semiconductor or insulator in another, show ferromagnetism potentially applicable for spin injection.[31]

These theoretical results motivate experimentalists to develop new synthesis routes for 2D high-temperature spin-polarized materials with ferromagnetism or antiferromagnetism for potential spintronic applications. However, such properties are yet to be experimentally confirmed, and their applications in spintronics remain limited by the lack of intrinsic magnetism of MXenes. Making matters worse, experimental studies on the magnetic behavior of MXenes are few and far between. Nevertheless, magnetism has been experimentally identified in 2D MXenes such as $Cr_2TiC_2T_x$ (but not in its parent 3D MAX phase),[32] Mn_3N_2 (even at 300 K),[33] and $Ti_3C_2T_x$ (functionalized *via* treatment with hydrofluoric and chlorosulfonic acid).[34] The last study has also shown that the magnetic properties of MXenes are affected by their surface terminal groups.[34] In turn, the distribution of these terminal groups is affected by the etching conditions and post-synthetic treatments applied to prepare these materials.[14–19] Therefore, we aimed at studying the relative contribution of these factors while experimentally testing the theoretically predicted electromagnetic properties of V_2CT_x[28] as a model MXene.

Combining both experimental and theoretical approaches, we conducted a detailed study of the magnetic properties of V_2CT_x MXene. In our study, V_2CT_x materials were prepared by wet etching, applying different acid concentrations and post-synthetic treatment in oxygen flow to modify the terminal groups (the ratio between O and F groups; O/F ratio) and to assess their effect on MXene magnetism. These materials were obtained in the form of multilayered powders and ultrathin films and characterized by powder X-ray diffraction (PXRD),

scanning transmission electron microscopy (STEM), and X-ray photoelectron spectroscopy (XPS), in addition to magnetic measurements. The experimental data were compared with DFT simulations to gain insights into the magnetic behavior of V_2CT_x materials.

Results and discussion

Theoretical study

In this study, we explored the experimental feasibility of V_2CT_x. By DFT,[35] we theoretically investigated V_2CT_x MXenes with different surface terminations to predict their magnetic properties (details of the methodology in ESI†). For this purpose, we used the V_2CT_2 model consisting of $V_2CO_xF_{2-x}$ periodic 2D layers. On the surface of these MXenes, we considered two different "hollow" sites, which result in three types of surface functionalizations (Fig. 1), namely surface-terminating groups located (i) above the "hollow" site formed by three neighboring C atoms (type I site) or (ii) above the C atoms (type II site) and (iii) a combination of the previous two, upper and lower surfaces (type III site), respectively. The type I site had the lowest energy of all surface-terminating modes under consideration and, thus, was used to study the geometric, electronic and magnetic properties of functionalized V_2CT_2 MXenes. Testing various F:O ratios (2:0, 3:1, 1:1, 1:2, 1:3, and 0:2; Fig. S1, ESI†), we performed calculations with the (2 × 2 × 1) supercell (except for the 1:2 ratio). The results are summarized in Table S1, in ESI.†

As calculated, the formation energies (E_{form} defined in eqn (S1), ESI†) of functionalized V_2CF_2 and V_2CO_2 MXenes are relatively high (−4.13 and −4.89 eV, respectively) and represent the lower and upper bounds of mixed MXenes. In other words, the formation energies of all mixed $V_2CO_xF_{2-x}$ MXenes are within these bounds (Table S1, ESI†), indicating that strong chemical bonds are formed between V and surface functional groups. The stacking of individual layers is shown in Fig. S2 (ESI†). The interlayer distances of various $V_2CO_xF_{2-x}$ MXenes range from 0.218 to 0.246 nm in V_2CF_2 and V_2CO_2, respectively, corroborating previous findings (0.24 nm).[36] Also
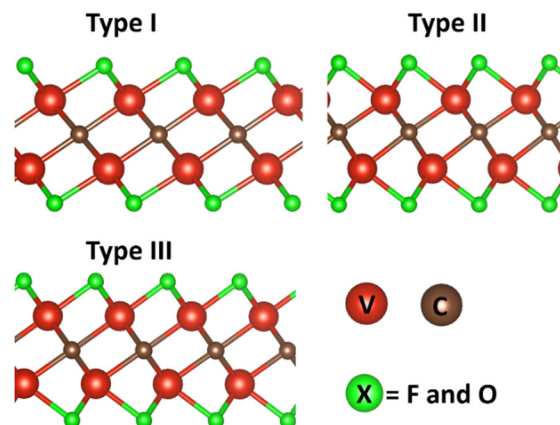

Fig. 1 Three possible binding sites for surface functionalization on V_2CT_2 MXenes.

in line with the experimental data and with previous reports,[37] the calculated lattice parameters of $V_2CO_xF_{2-x}$ MXenes (Table S1, ESI†) range from 0.295 to 0.316 nm.

Electronic states, spin polarization and magnetic properties were assessed for all $V_2CO_xF_{2-x}$ MXenes considered in this study (Fig. S1 and Table S1, ESI†). As shown by the potential magnetic configurations (Fig. S3, ESI†), the presence of O and F on the surface of MXenes leads to charge transfer towards the surface (Bader charge analysis).[38] This charge transfer affects the position of the V-3d orbitals in both spin channels. Our calculations of the local magnetic moments of V_2CO_2 revealed that V atoms are in a high spin state with 1 unpaired d electron (e.g., $d^1\uparrow$ spin configurations), corresponding to a V^{4+} electronic configuration. Thus, V_2CO_2 MXene is a ferromagnetic (FM) half-metal and has a total magnetic moment of $2\mu_B$ (per unit cell), which mainly derives from V atoms. In contrast, V_2CF_2 MXene is an antiferromagnetic (AFM) semiconductor, and its V atoms are in a high spin state with 2 unpaired d electrons (e.g., $d^2\uparrow$ spin configurations), formally corresponding to a V^{3+} electronic configuration. The calculated magnetic moments of V atoms increase with the concentration of surface F-functionalization, ranging from 1.12 (V_2CO_2) to $1.84\mu_B$ (V_2CF_2, see Table S1, ESI†).

Because the expected ratio between O and F functionalization is 2 : 1, the results from the $V_2CO_{1.5}F_{0.5}$ MXene model (with a 3 : 1 O/F ratio) are particularly relevant to experimental findings. All O and F configurations on the $V_2CO_{1.5}F_{0.5}$ MXene model (Fig. S1, ESI†) are found in the FM ground state. Using $V_2CO_{1.5}F_{0.5}$-C and $V_2CO_{1.5}F_{0.5}$-E MXenes as prototypes (the letters from C to E denote specific configurations of O/F surface atoms, as defined in Fig. S1, ESI†), we show their partial density of states (PDOS) in Fig. S4 (ESI†). In addition, spin-polarized densities are shown in Fig. S5 (ESI†) together with the variation of the heat capacity of $V_2CO_{1.5}F_{0.5}$ MXenes as a function of temperature calculated using Monte Carlo simulations. The corresponding Curie temperature is 7 K. The results show that not only spin polarization increases with the oxygen concentration but also the Curie temperature (T_C) increases with the asymmetry of surface functionalization in $V_2CO_{1.5}F_{0.5}$ MXenes. Accordingly, the Curie temperature can be engineered via surface functionalization.

We further considered four configurations of $V_2CO_{1.33}F_{0.67}$ MXenes modeled using a (3×3) supercell (Fig. S6, ESI†) with a 2 : 1 O/F ratio. All $V_2CO_{1.33}F_{0.67}$ MXenes are found in the ferromagnetic ground state and are half metals (Fig. S6, ESI†). To gain insights into the intriguing electronic properties of V_2CO_2, V_2CF_2 and $V_2CO_{1.33}F_{0.67}$ MXenes, PDOS of V-3d orbitals were plotted, as shown in Fig. S7a (ESI†). Given the local symmetry on V atoms of V_2CO_2 and V_2CF_2 MXenes, the V-3d orbitals split into a non-degenerate a (d_{z^2}) orbital and two 2-fold degenerate e orbitals, namely ($d_{yz} + d_{xz}$) and ($d_{x^2-y^2} + d_{xy}$). Both the conduction band minimum (CBM) and the valence band maximum (VBM) depend on the V-3d orbitals. The spin polarization of V-3d orbitals of $V_2CO_{1.33}F_{0.67}$ MXenes is stronger around the Fermi level than that of V_2CO_2 MXenes, but weaker in the deeper valence bands. Schematics of the spin

polarization of V atoms in symmetrically and asymmetrically functionalized surfaces are shown in Fig. S7b (ESI†). Due to the different chemical environments in functionalized $V_2CO_{1.33}$-$F_{0.67}$ MXenes, the non-degenerate V-3d orbitals result in the ferromagnetic spin state.

Varying the concentration of O and F on one of the surfaces provides an effective way to control the spin polarization of V atoms. Computational results indicate that the magnetic state of $V_2CO_xF_{2-x}$ MXenes is primarily determined by (i) the relative concentration of O and F surface atoms; all considered configurations of surface functional groups give the ferromagnetic state if the O/F ratio is above 2. But the relative stability of ferromagnetic and antiferromagnetic states is also modulated by (ii) the degree of asymmetry in the functionalization of upper and lower surfaces. Therefore, these two factors determine the magnetism of $V_2CO_xF_{2-x}$ MXenes.

Experimental section – preparation of V_2CT_x films

V_2CT_x MXene was first reported by Naguib et al. as a promising material for Li-ion batteries.[39] Its synthesis was subsequently improved by optimizing the conditions and stabilizing the exfoliated layers in a solution.[40] In the present study, we tested different etching conditions, combining hydrofluoric and hydrochloric acids in different concentrations at room temperature (≈ 24 °C) or 50 °C for 72 hours. We aimed to prepare films of V_2CT_x under different etching conditions and to assess the effect of the etching environment on their magnetic properties. Exposing MXenes to ambient air is known to spontaneously led to changes in terminal groups (typically halogen groups are replaced by oxygen groups)[41] and to undesired degradation of MXene layers. To prevent these alterations, all materials were stored either under vacuum or under argon atmosphere. They were analyzed shortly after their preparation under minimal exposure to ambient air, except during the oxidation treatment in which V_2CT_x films were purposely exposed to oxygen flow. The experimental conditions of V_2AlC etching are described in detail in ESI.† The materials prepared in this study and the corresponding experimental conditions are outlined in Table 1.

To exfoliate the layers, a freshly etched multilayered V_2CT_x (wet powder) was directly intercalated with a 25% tetramethylammonium hydroxide solution. Subsequent series of centrifugation and mechanical shaking yielded a black supernatant of exfoliated V_2CT_x layers. The exfoliated layers were immediately collected by filtration to prevent their degradation. Each material was denoted by the prefixes del (delaminated) and CA or DA depending on the etching conditions, as described in Table 1 (i.e. CA-del-V_2CT_x and DA-del-V_2CT_x). All thin films had a bronze hue. To demonstrate the reproducibility of etching in a diluted acid solution, we prepared delaminated films of V_2CT_x in two independent experiments to compare their properties and labeled them as DA-del-V_2CT_x (1) and DA-del-V_2CT_x (2). In their PXRD patterns (Fig. 2), all films have the same profile with similar intensities, and the (002) peak has the same position at 6.9° 2θ (corresponding to d-spacing 1.28 nm). Only DA-del-

Table 1 List of materials prepared in this study and the corresponding etching conditions, particularly the acid concentrations. The etching temperature (room temperature) and reaction time (72 hours) were identical in all experiments. Elemental analysis was based on XPS measurements; the materials were measured as a solid powder (DA-ml-V$_2$CT$_x$) and as thin films (with -del- designation). Materials highlighted in the same color are related to each other

| Material name	Composition (XPS)	Description	Etching conditions applied to parent V$_2$AlC (at room temperature, 72 hours)
DA-ml-V$_2$CT$_x$	V$_2$C$_{0.80}$F$_{0.96}$O$_{0.90}$	Multilayered powder	1 g V$_2$AlC + 12 ml 29M HF + 8 ml 6M HCl
DA-del-V$_2$CT$_x$ (1)	V$_2$C$_{0.71}$F$_{1.05}$O$_{1.02}$	Delaminated film – batch 1	1 g V$_2$AlC + 12 ml 29M HF + 8 ml 6M HCl
DA-del-V$_2$CT$_x$ (2)	V$_2$C$_{0.69}$F$_{1.06}$O$_{1.07}$	Delaminated film – batch 2	1 g V$_2$AlC + 12 ml 29M HF + 8 ml 6M HCl
DA-del-4O$_2$-V$_2$CT$_x$	V$_2$C$_{0.74}$F$_{0.88}$O$_{1.4}$	DA-del-V$_2$CT$_x$ (1) film treated for 4 hours in oxygen flow	1 g V$_2$AlC + 12 ml 29M HF + 8 ml 6M HCl
DA-del-8O$_2$-V$_2$CT$_x$	V$_2$C$_{0.71}$F$_{0.94}$O$_{1.08}$	DA-del-V$_2$CT$_x$ (1) film treated for 8 hours in oxygen flow	1 g V$_2$AlC + 12 ml 29M HF + 8 ml 6M HCl
CA-del-V$_2$CT$_x$	V$_2$C$_{0.65}$F$_{1.18}$O$_{0.77}$	Delaminated film	1 g V$_2$AlC + 12 ml 29M HF + 8 ml 12M HCl
CA-del-8O$_2$-V$_2$CT$_x$	V$_2$C$_{0.71}$F$_{0.87}$O$_{1.74}$	CA-del-V$_2$CT$_x$ film treated for 8 hours in oxygen flow	1 g V$_2$AlC + 12 ml 29M HF + 8 ml 12M HCl
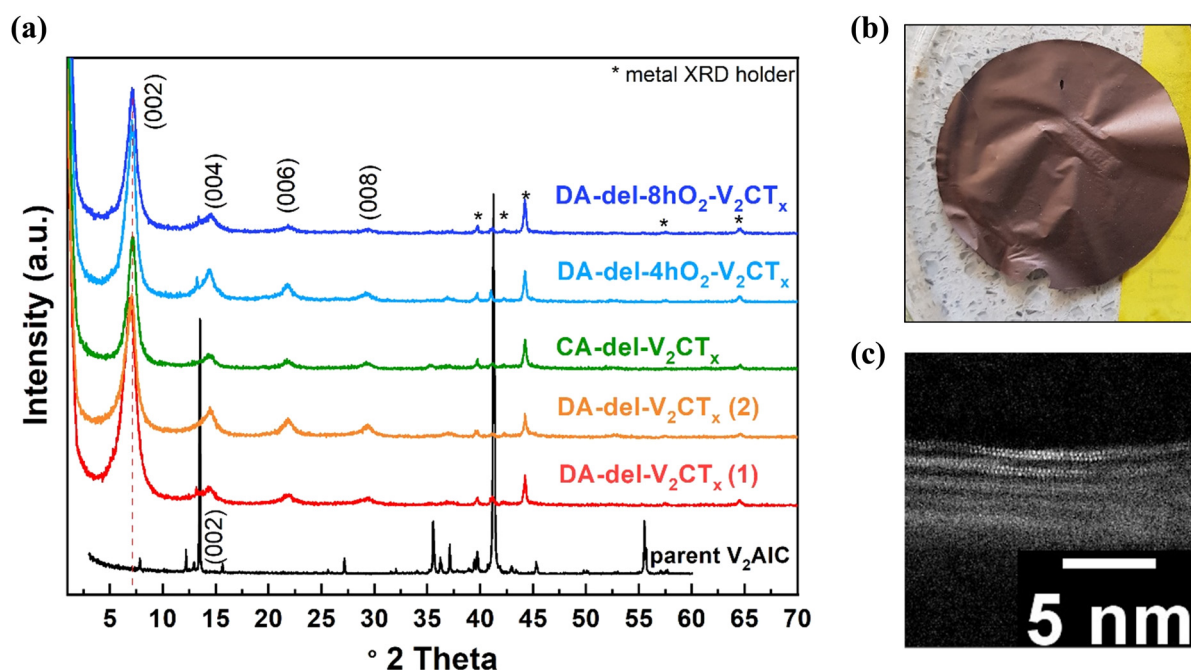
Fig. 2 (a) Comparison of PXRD patterns of delaminated V$_2$CT$_x$ thin films. Films prepared from multilayered V$_2$CT$_x$ after etching in concentrated acid solutions are indicated with the prefix CA. Films prepared using a diluted acid solution are indicated with the prefix DA. DA-del-V$_2$CT$_x$ were prepared in two batches, designated by (1) and (2). (b) Optical image of the DA-del-V$_2$CT$_x$ (1) thin film. (c) ADF-STEM image of DA-del-V$_2$CT$_x$ (1).

V$_2$CT$_x$ (1) shows low intensity peaks of the parent MAX phase, indicating a minor fraction of unreacted V$_2$AlC.

Characterization of V$_2$CT$_x$ films

STEM of V$_2$CT$_x$ films. By STEM, we characterized the delaminated V$_2$CT$_x$ materials (Fig. 3) using two approaches to sample preparation, namely (a) dropping the suspension of freshly delaminated V$_2$CT$_x$ onto the TEM grid, and (b) crushing a film prepared by filtration of the delaminated V$_2$CT$_x$ suspension before analyzing the sample. The STEM image of CA-del-V$_2$CT$_x$ (Fig. 3a) reveals a particle with holes across the flake. Fig. 3b shows a DA-del-V$_2$CT$_x$ (2) particle with a similar size, also riddled with holes and disruptions (more STEM images of

DA-ml-V$_2$CT$_x$ and DA-del-V$_2$CT$_x$ (1) are provided in ESI,† Fig. S11). The STEM image of DA-ml-V$_2$CT$_x$ included in Fig. S11 (ESI†) shows a block of crystallites with no obvious damage. Nevertheless, damage is more difficult to evaluate in a large, thick block of stacked layers than in a very thin flake in delaminated DA-del-V$_2$CT$_x$ (2) or CA-del-V$_2$CT$_x$. The delaminated materials prepared by etching with diluted acid contained smaller but more abundant holes than those prepared in concentrated acids. In both materials, the suspension of delaminated V$_2$CT$_x$ (CA-del-V$_2$CT$_x$, and DA-del-V$_2$CT$_x$ (2)) contained assemblies, most of which consisting of five to ten MXene layers, albeit with thinner assemblies and even a few monolayers as well. Furthermore, their interlayer distance analysis
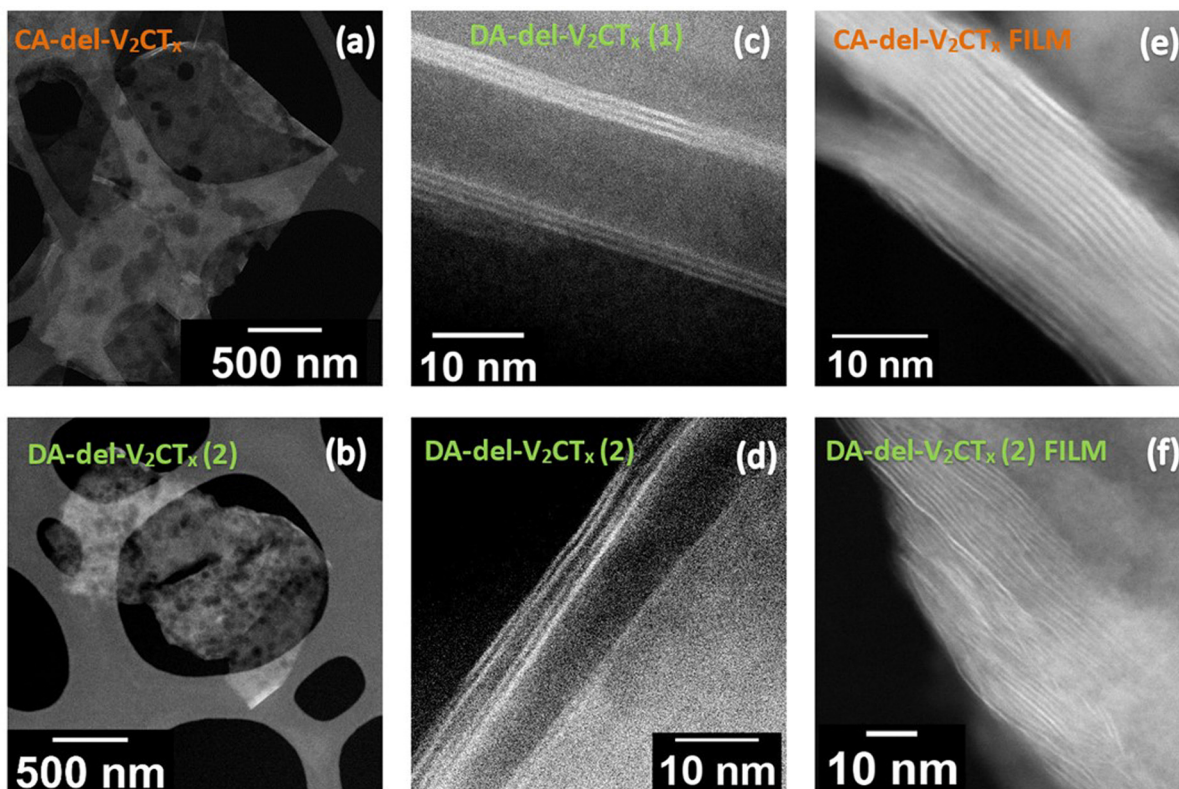
Fig. 3 Scanning transmission electron microscopy images of delaminated V_2CT_x analyzed (a)–(d) directly from the suspension of delaminated V_2CT_x (the delaminated V_2CT_x in the suspension was dropped onto the TEM grid directly after its preparation) and (e) and (f) as a film (after the filtration of the suspension, forming a thin film).

indicated the same d-spacing value, that is, 0.98 nm (d-spacing means the distance from the center of one layer to the center of the neighboring layer).

The films of delaminated V_2CT_x are displayed in Fig. 3e and f. In these films, the interlayer distance was 1.15–1.2 nm in DA-del-V_2CT_x (2) FILM and 0.97 nm in CA-del-V_2CT_x FILM. The d-spacing calculated from the (002) position in the PXRD pattern of the films was 1.28 nm. In contrast to these materials, the samples shown in Fig. 3c and d were prepared from the suspension of delaminated V_2CT_x, not the film. As determined by PXRD and STEM, the differences in d-spacing of the same films may be attributed to the treatment of these materials prior to analysis. For instance, the PXRD patterns of the films were measured on materials prepared by filtration of the suspension of delaminated V_2CT_x. As a result, the layer assemblies stacked on top of each other during the filtration.

Subsequently, the films were dried under vacuum, crushed into a powder and analyzed. As the delaminated V_2CT_x in suspension is dropped directly onto the holey-carbon copper TEM grid and then vacuumed under the STEM, water molecules between layers should more easily desorb (or de-intercalate) from a few layer assemblies than from films in which all layers are stacked on top of each other. As expected, when the films were crushed to a powder, deposited onto the TEM grid, and then exposed to high vacuum *in situ* within the STEM microscope, another portion of intercalated water molecules

was desorbed. This desorption is thought to be the main reason for the discrepancy between d-spacings calculated based on powder XRD patterns and those determined from STEM images.

Stability of V_2CT_x films in oxygen flow. This research aimed at unravelling the relationship between V_2CT_x surface functional groups and the magnetic properties of these materials. The degradation of MXenes materials or at least changes in their surface groups when they are exposed to air, moisture and/or light is often described in the literature,[40,42] as well as the effect of etching conditions on the composition of surface groups.[43] Based on our DFT study, the surface functional groups in V_2CT_x with an O/F ratio above 2 should induce a ferromagnetic state. To achieve such a significant change in functional groups while avoiding a complete oxidation of the MXene, we exposed selected del-V_2CT_x films to a stream of oxygen at room temperature (for 4 and 8 hours). By XPS analysis, we assessed changes in surface groups and chemical composition (for experimental details, see ESI†).

Aging of V_2CT_x film. To test V_2CT_x films with markedly different O/F ratios, we also stored the CA-del-V_2CT_x film for 10 months under vacuum in a desiccator. The PXRD pattern of the 10-month-old film was almost identical to that of a fresh CA-del-V_2CT_x sample (see Fig. S12, ESI†). Changes in terminal groups of the 10-month-old film were further promoted by treatment with oxygen flow for 8 hours. Once again, the PXRD

pattern did not reveal any significant change, but the XPS analysis showed that the composition of this film differed from that of the fresh film, as discussed in depth below.

XPS analysis of V_2CT_x materials. All materials were analyzed by XPS shortly after their preparation as published in a study by Vorotilo and Gogotsi[44] on the synthesis of the V_2AlC parent phase. By XPS, we can study the surface chemistry of materials into depths of 5–10 nm. In the C 1s spectra of all V_2CT_x materials, the C–V component at approximately 282 eV confirmed the presence of an MXene phase (Fig. S15, ESI†). Beyond qualitative insights into the MXene surface, quantitative XPS analysis enables us to determine the chemical composition of V_2CT_x materials. The ratio between the total vanadium photoemission signal and the carbon component ranged from 2.00 : 0.65 to 0.80 (Table 1), differing from the expected 2 : 1 ratio. Nevertheless, this discrepancy has also been described in other publications[39,43–45] and is likely related to multiple factors that impair the fit. These factors include the presence of oxygen in the carbon sublattice, defects introduced during the etching, the overlap of the V 2p signal with that of the O 1s signal, and the asymmetric shape of some components and satellites.

Multilayered powder DA-ml-V_2CT_x and the corresponding film, DA-del-V_2CT_x (1), have very similar chemical compositions, $V_2C_{0.80}F_{0.96}O_{0.90}$ and $V_2C_{0.71}F_{1.05}O_{1.02}$, respectively. In V 2p photoemission spectra of both materials, the strongest contribution is associated with V^{3+} at 515 eV (Fig. 4). The peak at 513 eV is attributed to V^{2+}, indicating the presence of an unreacted V_2AlC phase.[42,46] Traces of unreacted V_2AlC are also

visible in the XRD pattern of DA-ml-V_2CT_x and DA-del-V_2CT_x (1) (Fig. 2). However, the V–C peak overlaps at the same binding energy ($\sim$513 eV), which increases the peak.[42] The peak at $\sim$516 eV is assigned to the V^{4+} component of a monolayer of vanadium oxide on the surface of vanadium carbide.[39,42,46] The weak signal at $\sim$518 eV is assigned to the V^{5+} component, suggesting only minimal surface oxidation and thus the formation of vanadium oxide.

Two V_2CT_x films prepared under the same conditions, that is, treatment with diluted acids (DA-del-V_2CT_x (1) and DA-del-V_2CT_x (2)) had virtually identical chemical compositions and very similar XPS profiles (data fitting is shown in Table S2, ESI†). The similarity of these two samples prepared by repeating the etching procedure in diluted acid solutions supports the reproducibility of this etching protocol.

The CA-del-V_2CT_x film prepared in a concentrated acid solution had a higher concentration of fluorine groups and a lower concentration of oxygen groups, $V_2C_{0.65}F_{1.18}O_{0.77}$, than the films prepared in diluted acids, $V_2C_{0.69–0.71}F_{1.05–1.06}O_{1.02–1.07}$. In a previous study, the chemical stability of V_2CT_x materials has been tested by heating multilayered V_2CT_x powders up to 600 °C in nitrogen, carbon dioxide, air or hydrogen atmosphere, monitoring changes by Raman spectroscopy and XPS.[42] Here, we tested the stability of V_2CT_x films by exposing the films to oxygen for 4 and 8 hours. We applied only mild conditions at room temperature because we intended to replace fluorine groups on the V_2CT_x surface whilst avoiding vanadium oxidation into vanadium oxide. Our theoretical calculations indicated that V_2CT_x would be a ferromagnetic material if the
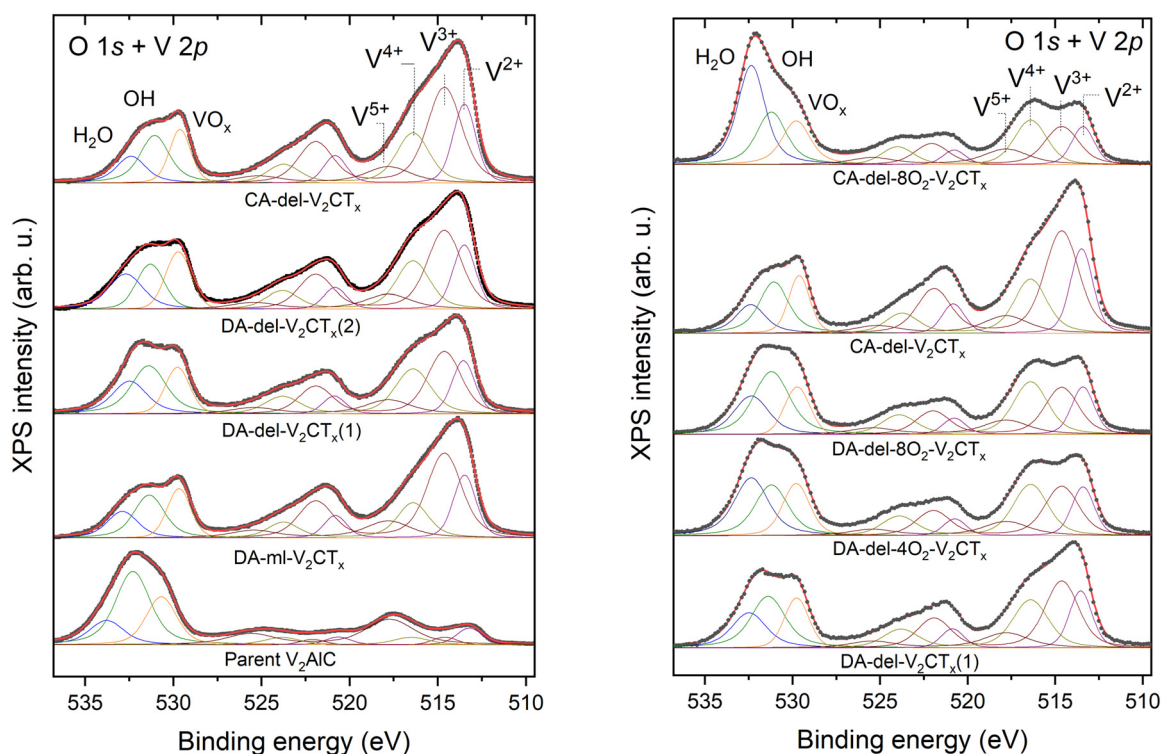

Fig. 4 Component peak-fitting of XPS spectra of parent V_2AlC, multilayered DA-ml-V_2CT_x and all delaminated films V_2CT_x.

oxygen groups prevailed on the surface (the computational findings are discussed above). Based on our XPS analysis, after 4 (DA-del-4O$_2$-V$_2$CT$_x$) and 8 (DA-del-8O$_2$-V$_2$CT$_x$) hours in oxygen flow, the films displayed only a slightly lower F/O ratio than fresh DA-del-V$_2$CT$_x$ (1) (see Table 1).

The V^{3+}/V^{5+} ratio can be used as an indicator of the undesired transformation of V$_2$CT$_x$ MXene into vanadium oxide. The fresh film DA-del-V$_2$CT$_x$ (1) has a V^{3+}/V^{5+} ratio of 2.98, but after 4 and 8 hours in oxygen, the films have V^{3+}/V^{5+} ratios of 2.51 and 2.3, respectively. This decrease in V^{3+}/V^{5+} ratio indicates that the concentration of vanadium oxide increases due to oxygen exposure. However, the concentration of fluorine groups remains relatively high (V$_2$C$_{0.71-0.74}$F$_{0.88-0.94}$O$_{1.08-1.4}$). After 10 months of storage in a desiccator, the film prepared in concentrated acid solution, CA-del-V$_2$CT$_x$, was also exposed to oxygen flow for 8 hours to assess surface changes. The V^{3+}:V^{5+} ratio significantly dropped from 4.02 to 1.79, and the overall composition changed from V$_2$C$_{0.65}$F$_{1.18}$O$_{0.77}$ to V$_2$C$_{0.71}$F$_{0.87}$O$_{1.74}$. This result demonstrates that the V$_2$CT$_x$ film is slowly degraded even when stored in a desiccator, but fluorine groups remain in the composition and are not arbitrarily exchanged for oxygen groups, as proposed in previous studies.[40,42]

Magnetic measurements. Magnetic properties of selected samples were investigated by superconducting quantum interference device (SQUID) magnetometry. The variation of molar susceptibility as a function of temperature, $\chi(T)$, is shown in Fig. 5. In line with previous reports,[47,48] the parent V$_2$AlC sample was not strongly affected by the variation in temperature, which is typical of metallic, Pauli paramagnetism. In turn, the V$_2$CT$_x$ samples revealed a temperature-dependent paramagnetic contribution, albeit with a striking difference between multi-layered DA-ml-V$_2$CT$_x$ and other delaminated thin film samples. While a dominant Curie-type paramagnetism is clearly visible in the $\chi(T)$ of DA-ml-V$_2$CT$_x$, the other $\chi(T)$ curves

show a superposition of the Curie and Pauli paramagnetism, as reported for differently functionalized multi-layered Ti$_3$C$_2$T$_x$ MXenes.[34] Here, the two components were analyzed by fitting the experimental data with the modified Curie–Weiss law:

$$\chi = \frac{C}{T - \theta_P} + \chi_0 \tag{1}$$

where χ stands for the molar magnetic susceptibility; C, for the Curie constant; θ_P, for the paramagnetic Curie temperature; and χ_0, for the temperature-independent Pauli contribution. In a fully localized system, χ_0 limits to zero, and the term (1) follows the standard Curie–Weiss law, while for the paramagnetism due to conduction electrons, C limits to zero, and only the Pauli term remains.

For samples with realistic C values, the effective magnetic moment was calculated using the following formula:

$$\mu_{eff} = \sqrt{\frac{3k_B C}{N_a \mu_0 \mu_B^2}} \tag{2}$$

where N_a stands for the Avogadro number; k_B, for the Boltzmann constant; μ_0, for the permeability of vacuum; and μ_B, for the Bohr magneton. Before the analysis, the molar magnetic susceptibilities calculated in different magnetic fields were compared to confirm the expected invariance. For the V$_2$AlC sample, the magnetic susceptibilities did not coincide, indicating ferromagnetic impurity. Thus, the molar susceptibility was corrected using the following formula:

$$\chi^{corr} = \frac{(\chi_1 B_1 - \chi_2 B_2)}{B_1 - B_2} \tag{3}$$

where μ_1 and μ_2 stand for the molar magnetic susceptibilities in two different magnetic fields, B_1 and B_2.

The parameters derived from the fit of the modified Curie–Weiss law are outlined in Table S3 (ESI†). Our analysis confirmed that Pauli paramagnetism occurs in V$_2$AlC
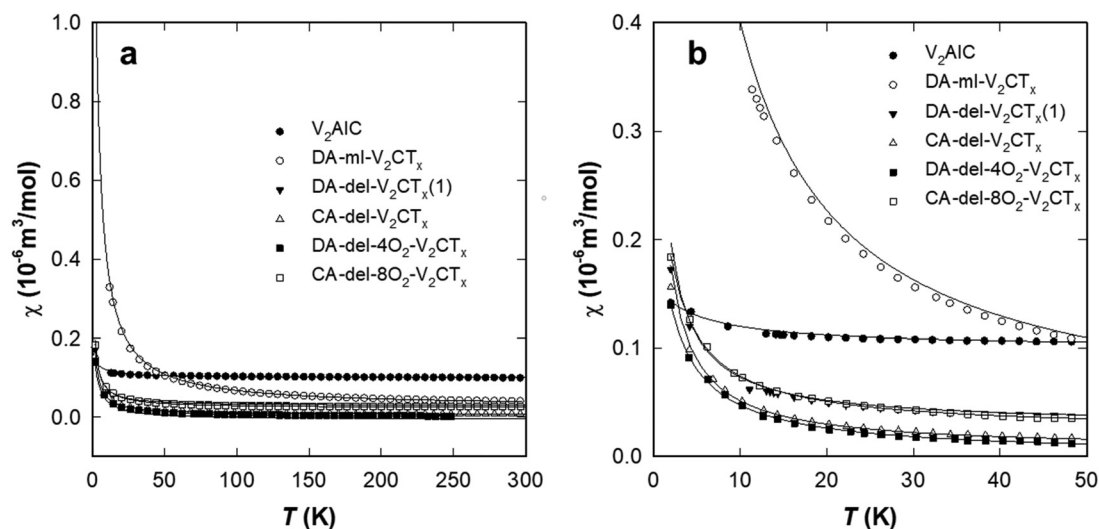

Fig. 5 Variation of the molar susceptibility as a function of temperature, $\chi(T)$. Panel (a) shows the full temperature range, while panel (b) corresponds to the low temperature − low susceptibility region, which reveals fine details between individual samples.
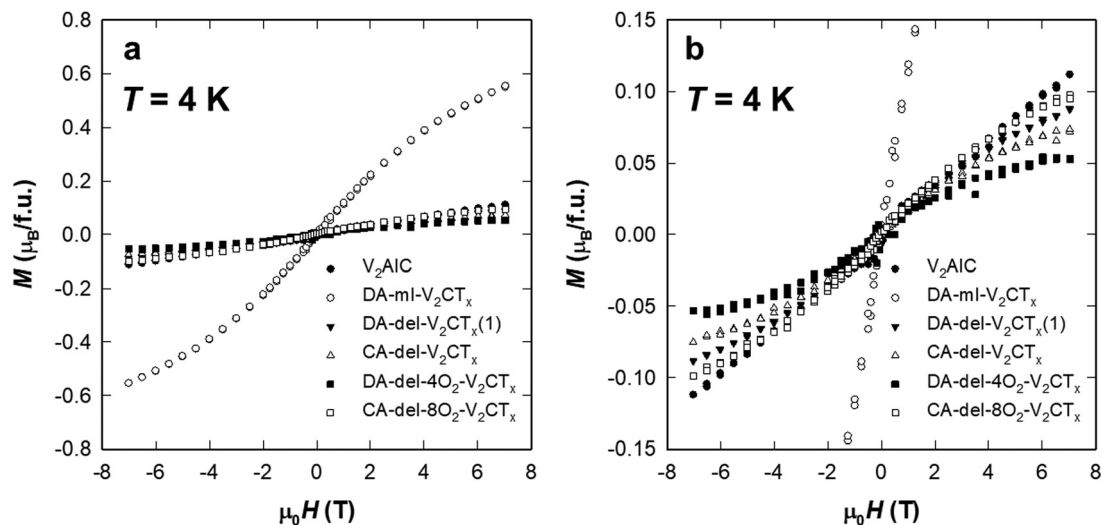
Fig. 6 Magnetization isotherms recorded at 4 K. Panel (a) shows the full-scale range, while panel (b) corresponds to the low magnetization region, which reveals fine details between individual samples.

($\chi_0 = 9.3 \times 10^{-8}$ m^3 mol^{-1}) and that localized paramagnetism prevails in multi-layered DA-ml-V$_2$CT$_x$, with $\mu_{eff} = 1.67\mu_B$, which is close to the theoretical spin-only value of the free V^{4+} ion ($1.73\mu_B$). In the samples with "mixed" paramagnetism, μ_{eff} ranges from 0.55 to $0.61\mu_B$, and χ_0 ranges from 2.3×10^{-9} to 2.9×10^{-8} m^3 mol^{-1}. In all samples with Curie paramagnetism, the θ_P values are <2 K, which is consistent with the absence of a long-range magnetic order down to 2 K.

The magnetization isotherms, $M(H)$ recorded at 4 and 300 K, shown in Fig. 6 and Fig. S13 (ESI†), respectively, corroborate the proposed scenario. The $M(H)$ of V$_2$AlC is almost identical at both temperatures, as expected for temperature-independent Pauli paramagnetism. A closer inspection of the $M(H)$ curve around the origin reveals moderate hysteresis ($\sim$50 mT), which may be attributed to ferromagnetic impurity revealed by molar susceptibility analysis. The $M(H)$ of DA-ml-V$_2$CT$_x$, recorded at 4 K has a clear Brillouin-type character, reaching $\sim$0.6μ_B f.u.$^{-1}$ at 7 T, while the other samples reach much lower values ($\sim$0.05–0.1μ_B f.u.$^{-1}$ at 7 T), as expected for "mixed" paramagnetism.

Based on our XPS analysis (Table 1), multilayered DA-ml-V$_2$CT$_x$ powder has a similar chemical composition to that of the thin film DA-del-V$_2$CT$_x$ (1), which was prepared from DA-ml-V$_2$CT$_x$ by organic intercalation and delamination (V$_2$C$_{0.80}$F$_{0.96}$O$_{0.90}$ vs. V$_2$C$_{0.71}$F$_{1.05}$O$_{1.02}$, respectively). In both samples, the ratio between F and O groups is approximately 1:1. Nevertheless, the DA-ml-V$_2$CT$_x$ powder displays localized paramagnetism, with $\mu_{eff} = 1.67\mu_B$, while the thin film DA-del-V$_2$CT$_x$ (1) shows "mixed" (metallic and localized) paramagnetism with $\mu_{eff} = 0.55\mu_B$. These differences in magnetic properties may be explained by differences in the integrity of crystallites as thin films crystallites contain numerous holes and cracks (evidenced by STEM images).

The main difference in chemical composition was identified between the fresh film CA-del-V$_2$CT$_x$ and the same film after 10 months (and additionally after 8 hours in oxygen flow) CA-del-

8O$_2$-V$_2$CT$_x$ (V$_2$C$_{0.65}$F$_{1.18}$O$_{0.77}$ vs. V$_2$C$_{0.71}$F$_{0.87}$O$_{1.74}$, respectively). Even when significantly varying the O/F ratio from 0.65:1 to 2:1, the two films displayed similar magnetism, that is, mixed paramagnetism, with effective magnetic moments of 0.56 and 0.61μ_B, respectively.

Although *ab initio* calculations usually predict a localized magnetic moment on V and a long-range magnetic order aligned with temperatures from units to tens of Kelvin,[48] our experimental results rule out a ferromagnetic or antiferromagnetic order of localized magnetic moments on V. Instead, most V$_2$CT$_x$ samples revealed superposition of metallic (Pauli) and localized paramagnetism, except for multi-layered DA-ml-V$_2$CT$_x$, nearing localized magnetism. This magnetic behavior can be understood considering the complexity of materials, in contrast to idealized theoretical models. Real samples contain various types of defects, local functionalization inhomogeneities and holes and cracks in crystallites (as evidenced by microscopy). Thus, the stable, long-range magnetism of fully localized spins is most likely suppressed by the intrinsic structural and spin disorder. Moreover, the magnetic properties are more affected by the crystallite sizes, shapes and the level of their disruption (for instance, holes and cracks) than by the actual chemical composition (particularly O/F ratio).

Ultimately, inconsistencies between experimental observations and theoretical predictions underscore the need for a more realistic description of magnetism in such complex materials. However, the level of crystallite damage during the etching and delamination process is difficult to predict. For now, this task remains highly challenging, if not impossible.

Conclusions

DFT calculations indicate that multi-layered and ultrathin film Vanadium MXenes, V$_2$CT$_x$, are ferromagnetic or antiferromagnetic depending on the relative concentration of oxygen and fluorine surface atoms. Nevertheless, the corresponding V$_2$CT$_x$

materials do not display the predicted behavior. Chemical analysis and magnetic measurements highlight the importance of the preparation pathway rather than the actual chemical composition and form of V_2CT_x MXene. Films with strikingly different chemical compositions (in terms of O/F ratio) show matching magnetism. Conversely, materials with virtually identical chemical compositions differ in their magnetism whether they are powders or films, most likely due to the generation of additional defects and cracks and to the disruption of crystallites during the intercalation and exfoliation processes. Similarly, the magnetic properties may be affected by the size and shape of the crystallites. Therefore, tapping into the potential of MXenes predicted by many theoretical studies requires developing experimental procedures for preserving MXene crystallites as intact as possible whilst enabling targeted modifications of surface terminal groups.

Experimental

V_2AlC MAX phase was purchased from Laizhou Kai Kai Ceramic Materials Co., Ltd.

Etching

Concentrated HF (29 M) and concentrated (12 M) or diluted (6 M) HCl were mixed in a plastic container. The acidic solution was cooled down to approximately 0 °C in an ice bath. The MAX phase V_2AlC was added in small portions to prevent undesired overheating and oxidation (1 gram was added over a period of 30 minutes), ensuring an appropriate and stable stirring, which is a crucial requirement. The ratios between the MAX phase and the acid solutions were 1 gram per 12 ml of 29 M HF and 8 ml of 12 M or 6 M HCl. The reaction vessel was loosely covered with a plastic top with two holes to allow the hydrogen gas to escape. The reaction was performed at 50 °C in an oil bath or at room temperature (24 °C) for 72 hours. After the reaction, the solid powder was separated through several cycles of centrifugation, decantation and deionized water addition until reaching pH 5–6. The solid fraction was subsequently separated by filtration using PVDF membrane filters. The multilayered V_2CT_x (ml-V_2CT_x) was designated by the prefix CA when using concentrated acid solutions for etching and by the prefix DA when using concentrated HF and diluted HCl.

Intercalation of tetramethylammonium cations and delamination

The freshly etched multilayered ml-V_2CT_x was directly mixed with a 25 wt% tetramethylammonium hydroxide solution (TMA-OH), and the mixture was stirred at room temperature for 6 hours (ratio 1 gram + 4 ml TMA-OH +16 ml H_2O). Then, the mixture was separated by centrifugation (3500 rpm for 10 minutes), subsequently discarding the first supernatant and adding fresh deionized water before subjecting the mixture to mechanical shaking for 4 minutes followed by centrifugation (2500 rpm for 10 minutes). The supernatant was then collected into a glass flask, repeating this cycle several times. Lastly, the supernatant was filtered using PVDF membrane filters, and the resulting del-V_2CT_x film was dried under vacuum at room temperature (for 24 hours). All films were stored under vacuum or in argon atmosphere.

Stability test in oxygen flow

A sample of the del-V_2CT_x film was treated in an oxygen flow 50–120 ml min^{-1} to test its stability and to assess the effect of oxygen on the terminal groups. For this purpose, the sample was loaded onto the frit bed and exposed to the stream of oxygen for 4 or 8 hours therein (see Fig. S11, ESI†). Subsequently, the film was directly analyzed by XRD and then stored under argon. The XPS and magnetic measurements were performed shortly thereafter. The materials were denoted by DA-del-$4O_2$-V_2CT_x and DA-del-$8O_2$-V_2CT_x. The sample CA-del-V_2CT_x was stored for 10 months under vacuum in a desiccator and then exposed to oxygen flow for 8 hours to compare the XPS spectra and the magnetic behavior of the fresh sample with those of the old sample exposed to oxygen. This sample was denoted by CA-del-$8O_2$-V_2CT_x.

Characterization

Powder XRD patterns were collected on a Bruker AXS D8 Advance diffractometer equipped with a DLYNXEYE XE-T detector in Bragg–Brentano geometry using Cu Kα (λ = 1.54056 Å) radiation operated at 30 mA and 40 kV. Data were collected in continuous mode over a 2θ range of 1–70°.

The chemical composition of the samples was measured on an X-ray photoelectron spectrometer equipped with a non-monochromatized Mg Kα X-ray source (1253.6 eV) and with a Phoibos 150 (SPECS GmbH, Germany) hemispherical analyzer operating in Fixed Analyzer Transmission (FAT) mode. After their preparation, the samples were kept under argon atmosphere for protection and mounted on a carbon double tape placed on a sample holder for XPS analysis. Survey spectra were collected at 40 eV pass energy, 0.5 eV step size, and 100 ms dwell time. Core-level spectra of O 1s, V 2p, N 1s, C 1s, F 1s, Cl 2p and Al 2p were collected at 20 eV pass energy, 0.05 eV step size and 100 ms dwell time. The satellite peaks from the non-monochromatized Mg X-ray source at 8.4 and 10.2 eV displacements and with 8.0 and 4.1% relative intensities, respectively, were filtered out of the spectra. The data were analyzed using KolXPD fitting software (KolXPD, Kolibrik.net, Czech Republic). All photoemission spectra were fitted with a mixture of Lorentzian and Gaussian function profiles after a Shirley background subtraction.

SEM images were obtained under a JEOL JSM-IT800 microscope using a secondary electron detector. Images were taken at a 1 kV accelerating voltage. All samples were deposited on conductive carbon tape mounted onto the SEM holder.

STEM images were acquired under a JEOL NEOARM 200 F microscope equipped with a Schottky-type field emission gun at 200 kV accelerating voltage, with annular dark-field (ADF) detector.

Details on the computational methods are described in ESI.†

The magnetic properties of the samples were measured using a properly calibrated MPMS XL-7 device (SQUID magnetometer, Quantum Design). Kept under an argon protective

atmosphere, the samples were rapidly transferred in a gelatine capsule, fixed in polystyrene onto a sample holder with a negligible background signal, and inserted inside the sample chamber of the magnetometer, which was evacuated and flushed with inert helium gas three times. The experiments were performed under helium gas exchange to enable fast sample thermalization. The variation of magnetization as a function of temperature, $M(T)$, was recorded at a constant magnetic field of 1, 2, and 4 T with a 2 K step after cooling the sample in the remnant field of the superconducting coil (below 0.5 mT). Magnetization isotherms, $M(H)$, were recorded at 4 K and 300 K under varying magnetic fields up to ±7 T with a 0.5 T step. All magnetization data were recalculated to the molar units using the mass determined from XPS experiments.

Author contributions

P. E., M. I. H. M., R. E. M. and P. N. conceived the research project and planned the experimental work. P. E. synthesized and characterized the materials and analyzed the data. B. Š. performed XPS measurements and data analysis. J. K. V. performed magnetic measurements and data analysis. M. M. and D. N. R. performed the STEM and SEM analysis, respectively. S. L., F. B., and P. N. performed simulations. The data were discussed among all co-authors. P. E. wrote the draft that was edited by all authors. All authors have approved the final version of this manuscript, except for P. N. who passed away in December 2022. The authors would like to dedicate this paper to his memory.

Conflicts of interest

There are no conflicts to declare.

Acknowledgements

Notes and references

1 K. S. Novoselov, A. K. Geim, S. V. Morozov, D. Jiang, Y. Zhang, S. V. Dubonos, I. V. Grigorieva and A. A. Firsov, *Science*, 2004, **306**, 666–669.

2 R. Z. Ma and T. Sasaki, *Adv. Mater.*, 2010, **22**, 5082–5104.

3 K. S. Novoselov, D. Jiang, F. Schedin, T. J. Booth, V. V. Khotkevich, S. V. Morozov and A. K. Geim, *Proc. Natl. Acad. Sci. U. S. A.*, 2005, **102**, 10451–10453.

4 S. Jeong, D. Yoo, J. T. Jang, M. Kim and J. Cheon, *J. Am. Chem. Soc.*, 2012, **134**, 18233–18236.

5 J. I. Dawson and R. O. C. Oreffo, *Adv. Mater.*, 2013, **25**, 4069–4086.

6 M. Naguib, M. Kurtoglu, V. Presser, J. Lu, J. Niu, M. Heon, L. Hultman, Y. Gogotsi and M. W. Barsoum, *Adv. Mater.*, 2011, **23**, 4248–4253.

7 A. VahidMohammadi, J. Rosen and Y. Gogotsi, *Science*, 2021, **372**, eabf1581.

8 X. Tang, X. Guo, W. Wu and G. Wang, *Adv. Energy Mater.*, 2018, **8**, 1801897.

9 Q. Zhu, J. Li, P. Simon and B. Xu, *Energy Storage Mater.*, 2021, **35**, 630–660.

10 A. Agresti, A. Pazniak, S. Pescetelli, A. Di Vito, D. Rossi, A. Pecchia, M. Auf der Maur, A. Liedl, R. Larciprete, D. V. Kuznetsov, D. Saranin and A. Di Carlo, *Nat. Mater.*, 2019, **18**, 1228–1234.

11 T. P. Nguyen, D. M. Tuan Nguyen, D. L. Tran, H. K. Le, D.-V. N. Vo, S. S. Lam, R. S. Varma, M. Shokouhimehr, C. C. Nguyen and Q. V. Le, *Mol. Catal.*, 2020, **486**, 110850.

12 X. Fan, Y. Yang, X. Shi, Y. Liu, H. Li, J. Liang and Y. Chen, *Adv. Funct. Mater.*, 2020, **30**, 2007110.

13 M. Han, D. Zhang, C. E. Shuck, B. McBride, T. Zhang, R. Wang, K. Shevchuk and Y. Gogotsi, *Nat. Nanotechnol.*, 2023, **18**, 373–379.

14 B. Anasori, M. R. Lukatskaya and Y. Gogotsi, *Nat. Rev. Mater.*, 2017, **2**, 16098.

15 V. Kamysbayev, A. S. Filatov, H. Hu, X. Rui, F. Lagunas, D. Wang, R. F. Klie and D. V. Talapin, *Science*, 2020, **369**, 979–983.

16 M. Seredych, C. E. Shuck, D. Pinto, M. Alhabeb, E. Precetti, G. Deysher, B. Anasori, N. Kurra and Y. Gogotsi, *Chem. Mater.*, 2019, **31**, 3324–3332.

17 I. Persson, L.-Å. Näslund, J. Halim, M. W. Barsoum, V. Darakchieva, J. Palisaitis, J. Rosen and P. O. Å. Persson, *2D Mater.*, 2018, **5**, 015002.

18 J. L. Hart, K. Hantanasirisakul, A. C. Lang, B. Anasori, D. Pinto, Y. Pivak, J. T. van Omme, S. J. May, Y. Gogotsi and M. L. Taheri, *Nat. Commun.*, 2019, **10**, 522.

19 I. Persson, J. Halim, T. W. Hansen, J. B. Wagner, V. Darakchieva, J. Palisaitis, J. Rosen and P. O. Å. Persson, *Adv. Funct. Mater.*, 2020, **30**, 1909005.

20 W. Hong, B. C. Wyatt, S. K. Nemani and B. Anasori, *MRS Bull.*, 2020, **45**, 850–861.

21 N. C. Frey, J. Wang, G. I. Vega Bellido, B. Anasori, Y. Gogotsi and V. B. Shenoy, *ACS Nano*, 2019, **13**, 3031–3041.

22 J. He, G. Ding, C. Zhong, S. Li, D. Li and G. Zhang, *Nanoscale*, 2019, **11**, 356–364.

23 J. J. He, P. B. Lyu, L. Z. Sun, A. M. Garcia and P. Nachtigall, *J. Mater. Chem. C*, 2016, **4**, 6500–6509.

24 J. J. He, P. B. Lyu and P. Nachtigall, *J. Mater. Chem. C*, 2016, **4**, 11143–11149.

25 J. J. He, G. Q. Ding, C. Y. Zhong, S. Li, D. F. Li and G. Zhang, *Nanoscale*, 2019, **11**, 356–364.

26 X. Yang and S. Dong, *J. Chem. Phys.*, 2024, **160**, 014705.

27 M. Khazaei, A. Ranjbar, M. Arai, T. Sasaki and S. Yunoki, *J. Mater. Chem. C*, 2017, **5**, 2488–2503.

28 J. P. Hu, B. Xu, C. Y. Ouyang, S. Y. A. Yang and Y. G. Yao, *J. Phys. Chem. C*, 2014, **118**, 24274–24281.

29 C. Si, J. Zhou and Z. M. Sun, *ACS Appl. Mater. Interfaces*, 2015, **7**, 17510–17515.

30 H. Kumar, N. C. Frey, L. Dong, B. Anasori, Y. Gogotsi and V. B. Shenoy, *ACS Nano*, 2017, **11**, 7648–7655.

31 Y. Li, M. Lai, M. Hu, S. Zhao, B. Liu and J.-J. Kai, *Sustainable Mater. Technol.*, 2022, **34**, e00516.

32 K. Hantanasirisakul, B. Anasori, S. Nemsak, J. L. Hart, J. Wu, Y. Yang, R. V. Chopdekar, P. Shafer, A. F. May, E. J. Moon, J. Zhou, Q. Zhang, M. L. Taheri, S. J. May and Y. Gogotsi, *Nanoscale Horiz.*, 2020, **5**, 1557–1565.

33 X. Xiao, P. Urbankowski, K. Hantanasirisakul, Y. Yang, S. Sasaki, L. Yang, C. Chen, H. Wang, L. Miao, S. H. Tolbert, S. J. L. Billinge, H. D. Abruña, S. J. May and Y. Gogotsi, *Adv. Funct. Mater.*, 2019, **29**, 1809001.

34 B. Scheibe, K. Tadyszak, M. Jarek, N. Michalak, M. Kempiński, M. Lewandowski, B. Peplińska and K. Chybczyńska, *Appl. Surf. Sci.*, 2019, **479**, 216–224.

35 G. Kresse and J. Hafner, *Phys. Rev. B: Condens. Matter Mater. Phys.*, 1993, **47**, 558–561.

36 H. Tan, C. Wang, H. Duan, J. Tian, Q. Ji, Y. Lu, F. Hu, W. Hu, G. Li, N. Li, Y. Wang, W. Chu, Z. Sun and W. Yan, *ACS Appl. Mater. Interfaces*, 2021, **13**, 33363–33370.

37 A. Champagne, L. Shi, T. Ouisse, B. Hackens and J.-C. Charlier, *Phys. Rev. B*, 2018, **97**, 115439.

38 G. Henkelman, A. Arnaldsson and H. Jónsson, *Comput. Mater. Sci.*, 2006, **36**, 354–360.

39 M. Naguib, J. Halim, J. Lu, K. M. Cook, L. Hultman, Y. Gogotsi and M. W. Barsoum, *J. Am. Chem. Soc.*, 2013, **135**, 15966–15969.

40 K. Matthews, T. Zhang, C. E. Shuck, A. VahidMohammadi and Y. Gogotsi, *Chem. Mat.*, 2022, **34**, 499–509.

41 J. Halim, K. M. Cook, M. Naguib, P. Eklund, Y. Gogotsi, J. Rosen and M. W. Barsoum, *Appl. Surf. Sci.*, 2016, **362**, 406–417.

42 R. Thakur, A. VahidMohammadi, J. Moncada, W. R. Adams, M. Chi, B. Tatarchuk, M. Beidaghi and C. A. Carrero, *Nanoscale*, 2019, **11**, 10716–10726.

43 R. Ibragimova, P. Rinke and H.-P. Komsa, *Chem. Mat.*, 2022, **34**, 2896–2906.

44 S. Vorotilo, C. E. Shuck, M. Anayee, M. Shekhirev, K. Matthews, R. W. Lord, R. Wang, I. Roslyk, V. Balitskiy, V. Zahorodna, O. Gogotsi and Y. Gogotsi, *Graph. 2D Mater.*, 2023, 93–105.

45 L.-Å. Näslund and I. Persson, *Appl. Surf. Sci.*, 2022, **593**, 153442.

46 A. VahidMohammadi, A. Hadjikhani, S. Shahbazmohamadi and M. Beidaghi, *ACS Nano*, 2017, **11**, 11135–11144.

47 C. M. Hamm, M. Dürrschnabel, L. Molina-Luna, R. Salikhov, D. Spoddig, M. Farle, U. Wiedwald and C. S. Birkel, *Mater. Chem. Front.*, 2018, **2**, 483–490.

48 S. Bae, Y. G. Kang, M. Khazaei, K. Ohno, Y. H. Kim, M. J. Han, K. J. Chang and H. Raebiger, *Mater. Today Adv.*, 2021, **9**, 100118.